Studies of impulsive vibrational influence on ultrafast electronic excitation transfer

Journal:	*The Journal of Physical Chemistry*
Manuscript ID:	Draft
Manuscript Type:	Article
Date Submitted by the Author:	n/a

Complete List of Authors:	Biggs, Jason; University of California, Chemistry Cina, Jeffrey; University of Oregon, Chemistry

Studies of impulsive vibrational influence on ultrafast electronic excitation transfer

Jason D. Biggs[†,‡] and Jeffrey A. Cina[*,†]

Department of Chemistry and Oregon Center for Optics, University of Oregon, Eugene, Oregon 97403, USA

E-mail: cina@uoregon.edu

[*]To whom correspondence should be addressed
[†]University of Oregon
[‡]Present address: Department of Chemistry, University of California, Irvine, California 92697-2025, USA

Submitted to J. Phys. Chem. A 30 September 2011

Abstract

We investigate electronic energy-transfer dynamics in three model dimers within which coherent intra-monomer nuclear motion has been induced by impulsive Raman excitation using an optimized, electronically pre-resonant control pulse. Calculations of the donor-survival probability, the ultrafast pump-probe signal, and the pump-probe difference signal are presented for dithia-anthracenophane and homodimers of 2-difluoromethylanthracene and 2-trifluoromethylanthracene. Survival probabilities and signals, along with phase-space analyses, elucidate the mechanisms, extent, and spectroscopic manifestations of external vibrational or torsional control over electronic excitation transfer.

Introduction

In a recent paper (Ref. 1, here referred to as Paper 1), we outlined a basic theory of vibrational control over electronic energy transfer (EET) and its spectroscopic observation by ultrafast two-dimensional electronic spectroscopy (2D ES) or the pump-probe limit of 2D ES. Paper 1 describes 2D ES in terms of the quantum mechanical overlap between nuclear wave packets which are shaped and transferred between different electronic potential energy surfaces by the action of ultrashort laser pulses or by energy transfer. That description—termed multidimensional (or nonlinear) wave-packet interferometry (md-WPI)—should be apposite to many situations of current interest in multidimensional spectroscopy involving the spectroscopic manifestations of coherent nuclear motion or its interplay with electronic dynamics.[2–28] A companion paper (Ref. 29, here called Paper 2) presented numerical simulations of the vibrational-control process and its observation by pump-probe spectroscopy in a variety of model EET systems.

A simplified model of the EET homodimer dithia-anthracenophane (DTA) was among the systems studied in Paper 2. EET in DTA, without prior vibrational excitation, has been a subject of detailed experimental[30] and theoretical[31] investigation. Our calculations on DTA[32] showed that selective impulsive Raman excitation of the lowest frequency vibration (the 385-cm^{-1} mode-12) of

the acceptor anthracene monomer by an optimally chosen transform-limited control pulse should discernibly influence the subsequent time-evolution of a short-pump-induced donor excitation and also the pump-probe difference signal. Interestingly, due to the small Franck-Condon displacement of mode-12 in the S_1 state of anthracene relative to the spatial width of the mode-12 vibrational wave packet, the influence is fairly small and opposite in sense to the simplest quasiclassical prediction (accelerating, rather than decelerating, short-time EET for the control-pump delay chosen in Paper 2).[33,34] Another model homodimer, featuring larger Franck-Condon displacement in a certain mode of the monomers, exhibited stronger vibrational control over EET in a direction consistent with quasiclassical predictions.[35]

The findings of Paper 2 motivate the present letter's exploration of two strategies for the enhancement of coherent vibrational control in realistic EET homodimers. We return to our dithiaanthracenophane model, termed DTA-12 for its inclusion of only mode-12 in both monomers, and investigate the extent to which larger vibrational displacements (hence more efficient control over EET) can be generated by impulsive Raman excitation with a linearly chirped, rather than transform-limited, control pulse. Using gas-phase laser-induced fluorescence and dispersed-fluorescence data as guides, along with ab initio electronic structure calculations, we explore the possibility of introducing stronger electronic-vibrational (or electronic-torsional) coupling within the anthracence-dimer complex by adding various fluorinated methyl substituents to both monomers. Calculations of donor-excitation survival probabilities and pump-probe difference signals as functions of the control-pump delay provide quantitative assessments of the effectiveness, mechanisms, and spectroscopic signatures of vibrational control of EET.

Setup

As in Paper 2, we consider various energy-transfer Hamiltonians of the form

$$H = |0\rangle H_0 \langle 0| + |1\rangle H_1 \langle 1| + \left|1'\right\rangle H_{1'} \left\langle 1'\right| + |2\rangle H_2 \langle 2| + J\left\{\left|1'\right\rangle\langle 1| + |1\rangle\left\langle 1'\right|\right\}, \qquad (1)$$

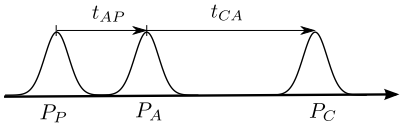

Figure 1: Three-pulse sequence of control-, pump-, and probe-pulse envelopes and interpulse delays. Subresonant control pulse P induces impulsive vibrational motion in a Raman-active intramonomer mode, while electronically resonant pump A and probe C initiate and monitor excited-state dynamics, respectively.

where $|0\rangle = |gg\rangle$, $|1\rangle = |eg\rangle$, $|1'\rangle = |ge\rangle$, and $|2\rangle = |ee\rangle$ are the ground, donor-excited, acceptor-excited, and doubly-excited site electronic states, respectively; H_j for $j = 0, 1, 1'$, and 2 are the corresponding nuclear Hamiltonians; and J is the EET coupling. We set $\hbar = 1$ throughout, so energy and angular-frequency units coincide. To Eq. (1) is added a time-dependent perturbation,

$$V(t) = -\sum_{I=P,A,C} \boldsymbol{\mu} \cdot \mathbf{E}_I(t), \tag{2}$$

accounting for the interaction of the EET complex with a subresonant control pulse, P, an electronically resonant pump pulse, A, and a resonant probe pulse, C, all of independently specified polarization, arrival time, duration, center frequency, and other characteristics. The dipole-moment operator appearing in Eq. (2) is taken to be the sum of those for the individual chromophores: $\boldsymbol{\mu} = \mathbf{m}(|1\rangle\langle 0| + |2\rangle\langle 1'|) + \mathbf{m}'(|1'\rangle\langle 0| + |2\rangle\langle 1|) + H.c.$ The pulse sequence is shown schematically in Figure 1.

All three pulses are Gaussian in shape. To include the possibility that the most effective control pulse might be chirped, we use laser fields of the form $\mathbf{E}_I(t) = \mathbf{e}_I E_I \mathrm{Re}\big(f_I(t) e^{-i\Phi_I(t)}\big)$, in which the pulse-envelope and phase functions are given by

$$f_I(t) = \frac{\sigma_I}{\sqrt{\sigma_I^2 + i\alpha_I}} \exp\Big\{-\frac{(t-t_I)^2}{2(\sigma_I^2 + (\alpha_I/\sigma_I)^2)}\Big\} \tag{3}$$

and

$$\Phi_I(t) = (t-t_I)\Omega_I + (t-t_I)^2 \frac{\alpha_I}{2(\sigma_I^4 + \alpha_I^2)}, \tag{4}$$

respectively.[36] E_I, $\mathbf{e}_I$, and t_I are the field strength, polarization unit vector, and arrival time of the I^{th} pulse, respectively. α_I is the chirp parameter, and σ_I is the pulse-duration parameter of a transform-limited pulse (i.e., one with $\alpha_I = 0$) having the same spectral intensity as the I^{th} pulse.

In order to define the nuclear Hamiltonians H_j appearing in Eq. (1) for a given EET dimer, one must specify the electronic potential energy surface for each electronic site-state. In addition, one has to give the energy-transfer coupling element, *J,* which may in general be nuclear-coordinate dependent. Ideally, one would perform ab initio electronic structure calculations on the full EET complex, and determine adiabatic potential energy surfaces and nonadiabatic couplings as functions of all relevant internal nuclear coordinates; such a program has largely been realized in a recent, thorough study on DTA itself.[31] Here we take a simpler, albeit less rigorous, approach by constructing model dimer Hamiltonians based on a Frenkel-exciton picture of single-site excitations in the isolated monomers.[37] We take the site excitation energies to be those of the isolated anthracene or substituted-anthracene moieties. As described further below, we ignore any nuclear-coordinate dependence of the EET coupling, and estimate its value from spectroscopic data (in the case of DTA[30,38]) or by scaling the DTA value using the transition dipole moments of individual substituted-anthracene monomers assigned to a DTA-like geometry. We further take advantage the ability of impulsive stimulated Raman scattering (ISRS)[39] to selectively excite the lowest-frequency Raman-active mode of a target chromophore: By constraining the control-pulse duration $\left(\sim \sqrt{\sigma_P^2 + (\alpha_P/\sigma_P)^2}\right)$ to be somewhat shorter than the period of each monomer's lowest-frequency Raman-active mode but longer than the periods of higher-frequency modes, so that its interaction with the EET dimer leaves the latter quiescent, we are able to make do with a simplified dynamical model that incorporates only this lowest-frequency internal vibrational or torsional degree of freedom in both anthracence or substituted-anthracene monomers.

Electronic Structure

The present study makes use of the same DTA-12 model of diathia-anthracenophane considered in Paper 2. DTA-12 is a homodimer incorporating a single, low-frequency 385-cm^{-1} a_g vibration

within each anthracene monomer,[40] displaced upon electronic excitation by $\delta_{12} \equiv d\sqrt{m\omega_{12}/2} = \sqrt{0.31}$;[38] the two molecular planes are assumed to be parallel to each other; the coupling element is $J = (16.8\,\mathrm{cm}^{-1})\exp(\delta_{12}^2) = 22.9\,\mathrm{cm}^{-1}$;[29] and, for simplicity, the short-axis-polarized site-transition dipole moments are taken to be mutually perpendicular, rather than approximately so.[30] The second row of Figure 2 shows donor- and acceptor-excited site potentials for this system.

By virtue of its small δ-value, the Franck-Condon displacement of the 12-mode in anthracene (and DTA-12) is less than the spatial width of that mode's vibrational wave packet. In order to construct realistic model systems with stronger electronic-vibrational coupling, we add a fluorinated-methyl substituent to both anthracene monomers, graft these substituted anthracenes onto the DTA structure, and adopt scaled values for the EET coupling. The choice of substituents is informed by gas-phase fluorescence measurements on 2-methylanthracene,[41,42] which revealed that the minimum of the methyl-torsion potential in this system undergoes a 60° phase-shift upon excitation to the S_1 electronic state. Electronic structure calculations by Nakagaki and co-workers[42] showed that interactions between π molecular orbitals of the anthracene ring and the out-of-plane methyl hydrogens act to stabilize the ground-state conformation at a zero-degree torsion angle. In S_1 a similar interaction favors the rotated-methyl orientation.

We carried out electronic structure calculations on 2-difluoromethylanthracene (DFMA) and 2-trifluoromethylanthracene (TFMA) using GAUSSIAN.[43] The ground-state geometry of DFMA was optimized via density functional theory (DFT)[44] using the B3LYP hybrid functional[45] and a cc-PVDZ basis set.[46] A methyl-torsion angle θ can be defined as the dihedral angle between the planes containing atoms 1, 2 & 3 and 2, 3 & 4 (see Figure 2, third row), starting from the equilibrium geometry ($\theta = 106.60°$) and holding all other nuclear coordinates constant. S_0 and S_1 energies were found as functions of θ, using time-dependent density functional theory (TD-DFT) for the excited state.[47] As can be seen in the third row of Figure 2, these calculations predict that electronic excitation of the DFMA monomer should lead to a substantial force on the methyl-torsion coordinate at the Franck-Condon point and a shift in the potential-energy minimum to $\theta = 87.77°$. The calculated S_0 torsional frequency of the difluoromethyl group is 36.9 cm^{-1} (cor-

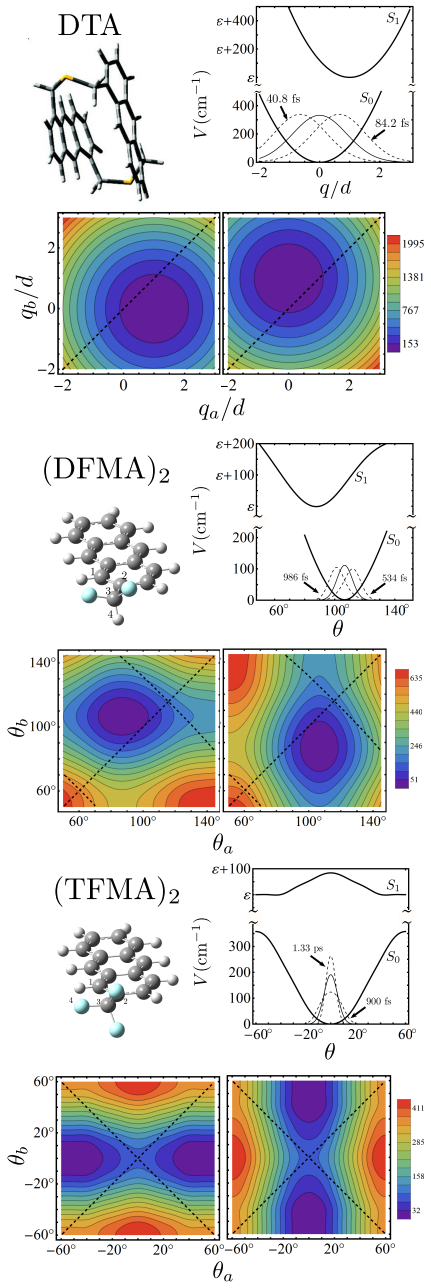

Figure 2: Each two-by-two panel shows: (Upper left) Optimized ground-state structure of dimer (DTA, this structure due to Jang and co-workers[31]) or monomer (DFMA and TFMA) for one of the EET models. (Upper right) Vibrational or torsional potential of lowest-frequency Raman-active mode in S_0 and S_1 states of monomer, along with ISRS-induced wave-packet dynamics (see text). (Lower left) 2D potential in donor-excited state (state 1) with respect to donor (abscissa) and acceptor (ordinate) intramonomer nuclear coordinates. (Lower right) 2D potential in acceptor-excited state (state 1′). Dashed lines locate intersections between state-1 and state-1′ potential-energy surfaces.

responding to a 904-fs librational period), and its Franck-Condon energy in S_1 is $68.5\,\mathrm{cm}^{-1}$. We may regard $\delta = 18.8^\circ/2\Delta\theta_{\mathrm{rms}} = 1.83$ as a measure of the torsional displacement, so this system features moderate electronic-nuclear coupling.

For TFMA, a slightly different procedure was employed. We used DFT with the B3LYP functional and a 6-31+G(d,p) basis set to determine the monomer's S_0 equilibrium geometry.[44,45,48] The minimum-energy conformation is predicted to mimic that of 2-methylanthracene: one C-F bond lies in the anthracene plane, corresponding to an equilibrium methyl-torsional angle $\theta = 0^\circ$. In order that our 1D torsional potential exhibit three-fold symmetry, we set all three C-F bond-lengths and F-C-F angles equal to the group-average value at the equilibrium geometry (the required changes in bond length were less than a tenth of the zero-point width of a C-F vibration). The S_0 and S_1 energies were found as functions of θ between -60° and 60° using TD-DFT for the excited state and freezing all other nuclear coordinates. Variation of θ did not appreciably alter the direction or magnitude of the calculated $S_1 - S_0$ transition dipole moment. The monomer electronic potential energy plots in the fifth row of Figure 2 give an $84.0-\mathrm{cm}^{-1}$ Franck-Condon energy for the trifluoromethyl torsion, whose calculated S_0 frequency is $\omega/2\pi c = 20.0\,\mathrm{cm}^{-1}$ (corresponding to a 1.67-ps librational period). The dimensionless displacement of this mode upon electronic excitation is $\delta = 60^\circ/2\Delta\theta_{\mathrm{rms}} = 5.4$, so it exhibits strong electronic-torsional coupling.

The energy-transfer coupling constants for the DTA-like dimers $(\mathrm{DFMA})_2$ and $(\mathrm{TFMA})_2$ were estimated by multiplying the spectroscopically derived J_{DTA} by the ratio of the squared norms of the transition dipoles for DFMA or TFMA and anthracene, calculated at the same level of theory.[49] That is,

$$J_{(\mathrm{DFMA})_2} \cong J_{\mathrm{DTA}} \frac{\boldsymbol{\mu}_{\mathrm{DFMA}} \cdot \boldsymbol{\mu}_{\mathrm{DFMA}}}{\boldsymbol{\mu}_{\mathrm{anth}} \cdot \boldsymbol{\mu}_{\mathrm{anth}}} = 16.8\,\mathrm{cm}^{-1} \times 0.819 = 13.2\,\mathrm{cm}^{-1} \tag{5}$$

and

$$J_{(\mathrm{TFMA})_2} \cong 16.8\,\mathrm{cm}^{-1} \times 0.907 = 15.2\,\mathrm{cm}^{-1}. \tag{6}$$

The bare electronic energy for the monomer $S_1 \leftarrow S_0$ transitions were determined by the methods

described above to be 25,970 cm^{-1} for DFMA and 26,158 cm^{-1} for TFMA; but the accuracy of these values is of no consequence for the energy-transfer calculations presented here, as we consider only homodimers, and each laser center-frequency is specified by its resonance offset. Note that, unlike the 385-cm^{-1} vibration in anthracene, the methyl librational frequencies in DFMA and TFMA are only slightly larger than the estimated EET coupling constant of the corresponding homodimer.

Dynamics

We performed dynamical and signal calculations for the three model systems by numerically diagonalizing the free-dimer Hamiltonian of Eq. (1) in the eigenbasis $\left\{\left|j\right\rangle\left|(n_a,n_b)_j\right\rangle\right\}$ of the uncoupled (J = 0) Hamiltonian; the exhibited basis element denotes a state in which the electronic degrees of freedom are in state j, while the vibrations (or librations) are in an eigenstate of H_j with n_a and n_b quanta in the donor and acceptor, respectively. The various reduced pulse propagators, $p_I^{(jk)}(t;\tau)$, which account for the reshaping of nuclear wave packets during electronic transitions, were calculated in the same basis with the neglect of EET (setting $J = 0$ in the integrand), but with full account of electronic-vibrational coupling (using the appropriate site-state potential function in H_j).[50] The basis was truncated at a certain total number of vibrational quanta. In DTA-12, with its small excited-state displacement, we took $(n_a + n_b) \leq 9$ and so kept 55 vibrational states in each electronic state. More states come into play in $(\mathrm{DFMA})_2$, but both torsional tunneling and barrier crossing can be safely neglected in this system. The cutoff was $n_a + n_b = 18$ for a total 190 vibrational states in each electronic state. Vertical electronic excitation of TFMA would copy the torsional wave packet to the top of an S_1 potential barrier. Although torsional tunneling could be neglected on the time-scales of interest, barrier crossing in the three-fold symmetric potential plays a significant role in the excited states, and many nuclear states must be retained to accurately represent the dynamics. We kept 5050 torsional levels in each of the four site-states of $(\mathrm{TFMA})_2$.

The basic mechanism of vibrational influence over EET explored in this letter is the same as that put forward in Papers 1 and 2. The strategy is to generate non-Franck-Condon initial states of

nuclear motion in the one-exciton manifold of the dimer in order to control the times, frequency, and duration for which the coherently evolving nuclear wave packet (in, say, the donor-state) comes into contact with intersections between donor-excited and acceptor-excited electronic potential energy surfaces (whose locations are indicated by dashed lines in Figure 2). It is at these loci of "resonant points" (including the Franck-Condon point in a homodimer) that surface-crossing energy-transfer transitions occur with greatest facility.[51,52] In Paper 2, we used ISRS to initiate coherent vibrational motion in the *acceptor* chromophore; in general this leads to a diagonal or anti-diagonal trajectory (or something in between) following short-pulse electronic excitation of the donor, which tends to avoid (or cross) the diagonal donor-acceptor intersection line. Because $(\mathrm{TFMA})_2$ (and to a lesser extent $(\mathrm{DFMA})_2$) are seen in Figure 2 also to possess dynamically accessible *anti*-diagonal intersection lines, we change tactics slightly in the present study and seek to initiate vibrational motion in the *donor* chromophore prior to its electronic excitation, with an eye to the possibility of trapping the short-pulse-excited wave packet in a well of the donor-excited site-state potential, thereby once again controlling its access to donor-acceptor intersection lines.

For each of the dimer complexes under study, we searched for the control-pulse parameters of center frequency Ω_P and duration σ_P (and in the case of DTA-12, also the pulse-chirp parameter α_P) that give rise to the largest-amplitude motion of the relevant low-frequency intramonomer vibrational or torsional mode in the electronic ground state. The search was carried out explicitly using a semianalytic form for the second-order action of the reduced pulse propagator,[29] subject to the constraint that the control-pulse-induced electronic excitation be less than a certain small percentage of the norm of the portion of the ground-state wave packet proportional to E_P^2.[53] For DTA, this search yielded optimal parameters $\Omega_P = \varepsilon - 1.58\omega_{12}$ (where ε is the bare electronic transition frequency), $\sigma_P = 0.217(2\pi/\omega_{12}) = 18.9\,\mathrm{fs}$, and $\alpha_P = -0.031(2\pi/\omega_{12})^2 = -234\,\mathrm{fs}^2$.[54] At $t - t_P = 0.47(2\pi/\omega_{12})\,(\mathrm{or}\,0.97(2\pi/\omega_{12}))$, the second-order wave packet in the affected monomer attains its largest negative (or positive) displacement $\langle q \rangle = \mp 0.63d$. Although the introduction of chirp increases the range of the impulsively induced vibrational motion over the $\langle q \rangle = \mp 0.54d$ achievable with a transform-limited control pulse,[29] the amplitude of motion ($0.70\Delta q_{\mathrm{rms}}$) remains

somewhat less than the width of the mode-12 wave packet.

Transform-limited control pulses were found to produce excitation of the torsional mode in $(\mathrm{DFMA})_2$ and $(\mathrm{TFMA})_2$ that is adequate for our purposes. For $(\mathrm{DFMA})_2$, $\Omega_P = \varepsilon - 60.2\,\mathrm{cm}^{-1}$ and $\sigma_P = 135.6\,\mathrm{fs}$ are the optimal parameters in the absence of chirp. With these pulse properties, impulsive Raman excitation is predicted to generate a coherent torsional oscillation of amplitude $\left|\langle\theta\rangle\right| = 4.67^\circ$ in the difluoromethyl group of the stimulated monomer, a full 90% of the corresponding 5.15° wave-packet width. The optimal control-pulse parameters for $(\mathrm{TFMA})_2$ place the center frequency $83.5\,\mathrm{cm}^{-1}$ below *vertical* resonance (at $\theta = 0^\circ$) with $\sigma_P = 183\,\mathrm{fs}$. Since there is a potential maximum at the Franck-Condon point of TFMA, the second-order torsional wave packet in S_0 undergoes breathing motion, rather than displacement, as its RMS width oscillates between 3.8° and 7.6°.[55]

The range of motion of the vibrational probability density corresponding to the ISRS-induced second-order wave packet is superimposed on the ground-state monomer potential curve plotted in Figure 2 for each of the model systems.

As a test of the effect of initial vibrational excitation on the time-course of EET following short-pulse electronic excitation, we consider the donor-survival probability, defined as

$$P_1(t) = \frac{\langle \psi_1(t) | \psi_1(t) \rangle}{\langle \psi_1(t_A) | \psi_1(t_A) \rangle}; \tag{7}$$

here $|\psi_1(t)\rangle$ is the nuclear amplitude remaining in the donor-excited state some time after the excitation to that state by pulse A of the second-order ground-state amplitude with ISRS-generated coherent vibrational motion in the donor chromophore.[56] Operationally, the quantity $P_1(t)$ is the pump-induced population of the donor-excited state derived solely from the portion of the ground-state wave packet that is second order in the control-pulse field strength for a sample of oriented dimers having one transition dipole moment parallel to the common polarization of the control and pump pulses (and the other perpendicular to it), relative to its value at $t = t_A$. Contour plots in Figure 3 show the survival probability for each of our EET models as a function of the time

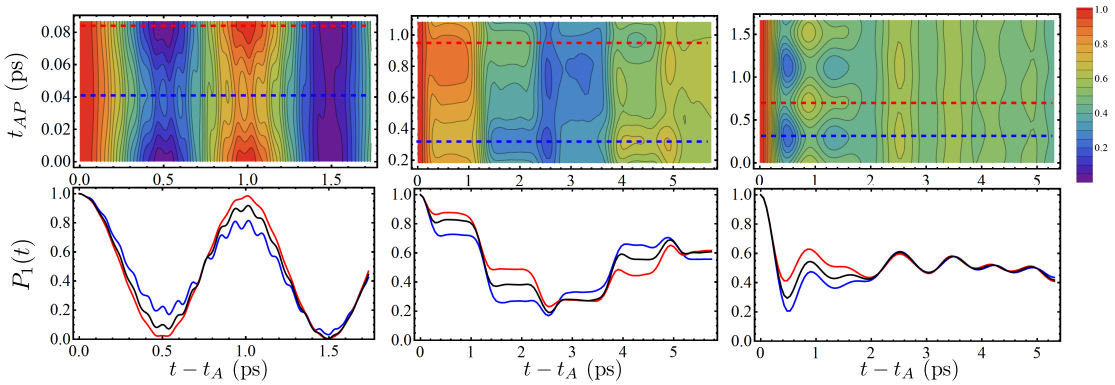

Figure 3: Left, middle, and right columns give donor-excited survival probabilites for DTA-12, $(\mathrm{DFMA})_2$, and $(\mathrm{TFMA})_2$, respectively, following short-pulse electronic excitation of donor a time t_{AP} after coherent impulsive excitation of its lowest-frequency Raman active mode. Upper panel in each column shows survival probability with respect to post-pump delay for a range of t_{AP} values. Lower panels plot $P_1(t)$ slices featuring maximal enhancement or diminuition of short-time EET (in blue and red), corresponding to control-pump delays indicated in upper panel, along with survival probability in the absence of prior vibrational excitation (black).

following donor excitation, for a range of control-pump delays. The control-pulse parameters for each system are those identified above. All pump (and, later, probe) pulses are transform limited.

The pump pulse used with DTA-12 is vertically resonant at the equilibrium position, with $\Omega_A = \varepsilon + \omega_{12}\delta_{12}^2$, and much shorter than a 12-mode vibrational period, with $\sigma_A = 0.1(2\pi/\omega_{12}) = 8.66\,\mathrm{fs}$. Survival-probability slices for values of the control-pump delay leading to the slowest (t_{AP} = 40.8 fs) and fastest (t_{AP} = 85.1 fs) initial loss due to energy transfer are shown in the lower left panel of Figure 3 along with the survival probability following Franck-Condon excitation by the same pump pulse of the unperturbed vibrational ground state. The evident variation of $P_1(t)$ with t_{AP} and the differences from the survival trace following Franck-Condon excitation show the extent of vibrational control over EET achieved in the dithia-anthracenophane system. Despite the slightly larger amplitude of coherent mode-12 vibration induced (in the donor) by a chirped control pulse, the effect on donor-excitation survival is not dramatically different from that calculated previously using a transform-limited control pulse (to induce coherent vibrational motion in the electronic excitation acceptor).[57]

In the present instance, the internal vibration of the acceptor chromophore is stationary before

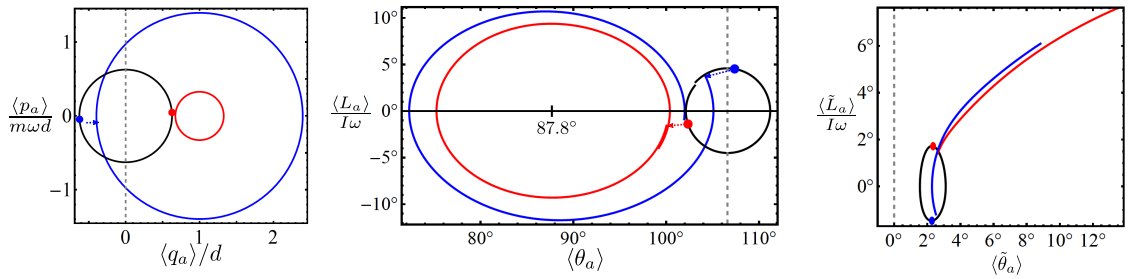

Figure 4: Phase-space trajectories plotting simultaneous expectation values of position (or angle) and momentum (or angular momentum) of relevant nuclear mode of donor chromphore in (left to right) DTA, $(\mathrm{DFMA})_2$, and $(\mathrm{TFMA})_2$. Black path shows Raman-induced motion in electronic ground state. Blue and red trajectories track wave-packet dynamics in donor-excited state following pump pulse at selected t_{AP} values identified in Figure 3. Excited-state expectation values are calculated in absence of EET (that is with J set to zero). Vertical dashed lines are at Franck-Condon point, which is also point of intersection between donor-excited and acceptor-excited site states when acceptor coordinate takes its ground-state equilibrium value.

and shortly after pump-pulse excitation of the donor, so we can gain insight by examining a plot of the "phase-space" trajectory tracking the simultaneous position and momentum expectation values of the donor vibration. The left-most panel of Figure 4 provides such a plot for DTA-12. The black circle shows the clockwise trajectory of the donor vibration in the electronic ground state. The large blue and small red circles describe the initial trajectories in the donor-excited state corresponding to survival traces of the same colors in Figure 3 (bottom-left panel). Since $\Delta q_{\mathrm{rms}} = \Delta p_{\mathrm{rms}}/m\omega \cong 0.90d$ for mode-12, the quantum mechanical distribution accompanying the blue phase-point actually spends *less* time overlapped with the surface-crossing line $q = 0$ during a vibrational period than that accompanying the red point, and EET is curtailed in the former case compared to the latter. The blue survival probability trace, corresponding to the larger-amplitude vibrational trajectory, also exhibits more pronounced vibrational quantum beating than the red one as a result of wave-packet motion out of and into the surface-crossing region.

The central panels of Figure 3 plot the survival probability for $(\mathrm{DFMA})_2$. We used a short pump ($\sigma_A = 90.4$ fs) that is resonant at $\theta = 100°$. The top-center panel gives a two-dimensional representation for $180\,\mathrm{fs} \leq t_{AP} \leq 1.08\,\mathrm{ps}$, while the bottom-center shows the individual survival-probability scans corresponding to maximal enhancement (blue, for $t_{AP} = 325.6$ fs) and diminution (red, for

t_{AP} = 940.6 fs) of short-time EET. In $(\mathrm{DFMA})_2$ the influence of the difluoromethyl libration on excitation transfer is substantial, and in keeping with the simplest quasiclassical predictions, due to the sizeable displacement, $18.8^\circ = 3.65\Delta\theta_{\mathrm{rms}}$, between the S_0 and S_1 potential minima relative to the angular width of the ground-state wave packet. The mechanism of this influence is illustrated in the middle panel of Figure 4. The wave packets giving rise to both blue and red excited-donor phase-space paths fully depart and later again approach the surface-crossing region $\theta \approx 106.6^\circ$. The cessation of EET during the absence of the wave packet from the crossing region accounts for the plateaus in $P_1(t)$. The blue trajectory spends more time near the crossing initially and penetrates the region more deeply on its return, leading to faster EET.

In the case of $(\mathrm{TFMA})_2$ we used a pump pulse of duration $\sigma_A = 147\,\mathrm{fs}$, electronically resonant at $\theta = \pm 7.4^\circ$ (the classical outer turning points of a torsional oscillator having the zero-point energy). The donor-survival probability for this system is displayed in the two right-most panels of Eq. (7). Nuclear control over EET is effective in this system due to its strong electronic-torsional coupling, as indicated by the significant variation with t_{AP} of the survival probability from ~ 0.5 to 2.0 ps after excitation. The fastest (slowest) short-time EET is seen for t_{AP} = 316.9 fs (700.5 fs).

$(\mathrm{TFMA})_2$ behaves differently from $(\mathrm{DFMA})_2$ in several interesting respects. As we have seen, the RMS width, rather than the expectation value, of the torsion-angle coordinate of the donor chromophore is set in motion by ISRS (it oscillates at *twice* the ground-state librational frequency). The phase-plot in the right-most panel of Figure 4 shows donor angular and angular momentum expectation values from the portion of the wave packets confined to the restricted range $0^\circ \leq \theta \leq 120^\circ$. In addition, the excited-state librational dynamics of the trifluoromethyl group is slower than energy transfer and highly anharmonic. The classical round-trip time for an oscillator placed on the S_1 potential at $\theta = 7.7^\circ$ is 4.4 ps, whereas $2\pi/J = 2.19\,\mathrm{ps}$. Thus, a large amount of excitation transfer occurs before the donor torsional wave packet leaves the Franck-Condon region. In fact, the full range of donor population loss, from maximally accelerated (blue) to maximally decelerated (red) can be explained by the delayed or hastened departure from that region, respectively; this can be seen from the corresponding phase-space trajectories in Figure 4, which show only

the first 667 fs of excited-state evolution. After a half-period of motion in the donor-excited state, wave-packet spreading renders the angular-coordinate distribution insensitive to initial conditions, and nuclear dynamics no longer influences electronic excitation transfer.

Signals

Although the donor-state survival probability (Eq. (7)) provides a useful theoretical metric for vibrational control over EET, it is important to identify signatures of vibrational control in observable spectroscopic signals. Accordingly, we next added a polarized probe pulse (C) to the control and pump pulses considered thus far and calculated pump-probe difference signals[1,29] from the three energy-transfer dimers. For our purposes, a pump-probe signal is the pump-induced change in the time- and frequency-integrated fluorescence from the single-exciton manifold generated by the probe pulse, which is assumed to be proportional to the portion of the expectation value of $|1\rangle\langle 1| + |1'\rangle\langle 1'|$ that is proportional to $E_A^2 E_C^2$.[58] The pump-probe difference signal—proportional to $E_P^2 E_A^2 E_C^2$—is then the pump-probe signal *with* minus that *without* a preceding control pulse.

As detailed in Paper 1 and illustrated in Paper 2, pump-probe and pump-probe difference signals can be calculated as sums of several contributing overlaps between nuclear wave packets generated and shaped by specific sequences of pulse- and excitation-transfer-induced transitions between and evolution upon the four electronic site-state potential surfaces. Signals from isotropic or oriented samples are obtained as sums of such overlaps, each weighted by an average over the appropriate orientational distribution of a certain product of cosines between a laser-polarization and a transition-dipole direction.[1,59] In contrast to the quantity $\langle \psi_1(t) | \psi_1(t) \rangle$ appearing in Eq. (7), the pump-probe difference signal has the advantageous feature of being proportional to the intensity ($\propto E_P^2$) of the control pulse, rather than its square. But there is a complicating feature too, as terms in the pump-probe difference signal appear in pairs, in which the second-order action of the control pulse is associated alternately with the bra or the ket in each contributing wave-packet overlap.[60,61]

Calculated pump-probe difference and pump-probe signals from an isotropic DTA-12 sam-

ple are plotted in the left column of Figure 5. For the pump-probe difference signal, an HHH polarization scheme is used in which horizontally polarized control and pump pulses, with characteristics listed above, are followed by a horizontally polarized probe pulse. An elongated $\sigma_C = 0.5(2\pi/\omega_{12}) = 43.3\,\text{fs}$ and red-shifted $\Omega_C = \varepsilon - 3\omega_{12}\delta_{12}^2$ were chosen to accentuate stimulated emission at the expense of ground-state bleach and excited-state absorption signal contributions—to the limited extent possible in this system with weak electronic-vibrational coupling. The left-middle panel shows traces at two control-pump delays giving rise to disparate pump-probe difference signals (purple for t_{AP} = 20.0 fs, teal for t_{AP} = 69.5 fs). As with the donor-survival in Figure 3, the range of pump-probe delays corresponding to a first interval of forth-and-back EET ($t_{CA} \sim 0\,\text{to}\,1\,\text{ps}$) exhibits the greatest variability in the pump-probe difference signal. Both selected pump-probe difference traces show prominent vibrational quantum beats throughout the displayed delay range. The lack of direct proportionality between the pump-probe difference signals and the HH-polarized pump-probe trace (left-bottom panel) by itself provides evidence for some degree of vibrational influence over short-time EET in DTA, as it manifests a discernible difference in form between the control-induced second-order wave packet and the vibrational ground-state wave function. The middle column in Figure 5 gives pump-probe difference and pump-probe signals for an isotropic sample of $(\text{DFMA})_2$, calculated with the parameters stated previously for H-polarized control and pump pulses and an H-polarized probe pulse of duration $\sigma_C = 90.4\,\text{fs}$ with its center frequency resonant at $\theta = 75.5^\circ$ (the outer turning point for nuclear motion in the excited state). Cuts from the 2D difference-signal plot for selected control-pump delays (purple for t_{AP} = 217.0 fs, teal for t_{AP} = 786.8 fs) are shown in the second panel of the middle column. Peaks in the pump-probe difference signal (and in the HH-polarized pump-probe signal shown the middle-bottom panel) occur when the torsional wave packet visits the outer turning-point region. Like the corresponding plateau regions in the survival probability (Figure 3), these delay ranges show the greatest variability with t_{AP}, especially the first two, which take place during the initial stepwise decrease in donor population. Spectral selection is effective in this system. For the chosen probe frequency, the calculated signals are largely dominated by the stimulated-emission contribution,

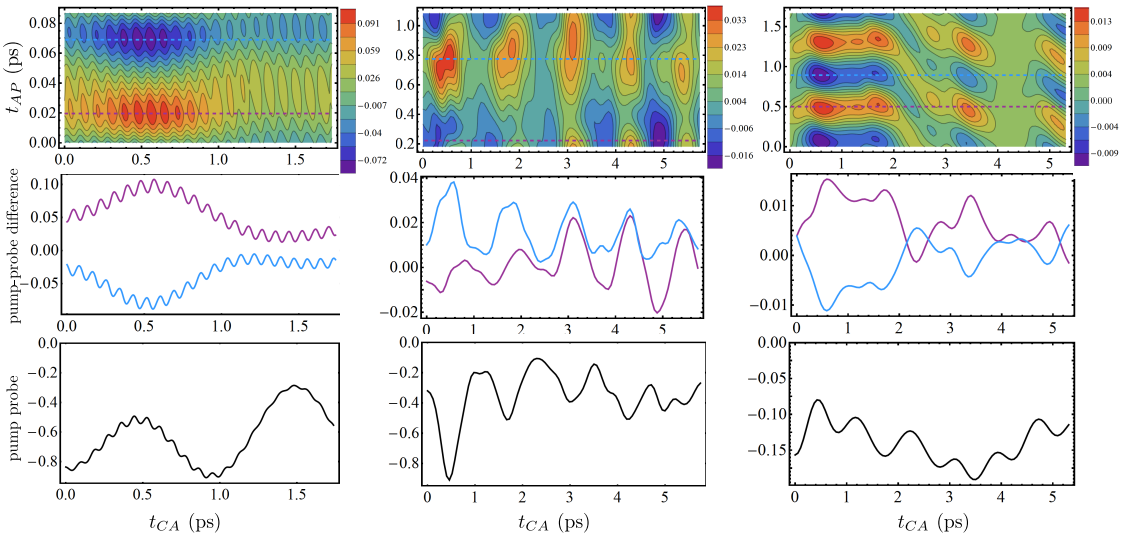

Figure 5: Calculated signals for DTA-12 (first column), $(\mathrm{DFMA})_2$ (second), and $(\mathrm{TFMA})_2$ (third). Top panel in each column displays HHH-polarized pump-probe difference signal (in units of $\sigma_P^2\sigma_A^2\sigma_C^2E_P^2E_A^2E_C^2m^6/2^6$) with respect to pump-probe delay t_{CA} for range of control-pump delays t_{AP}. Middle panels give pump-probe traces at selected t_{AP} values. Bottom panels plot HH-polarized pump-probe signals (no control pulse; in units of $\sigma_A^2\sigma_C^2E_A^2E_C^2m^4/2^4$). DTA and $(\mathrm{DFMA})_2$ samples are isotropic; $(\mathrm{TFMA})_2$ has one transition dipole parallel to H-axis.

with ground-state bleach and excited-state absorption (not shown separately) accounting for only a few percent of the plotted values. As expected given the moderate electronic-torsional coupling in $(\mathrm{DFMA})_2$, the pump-probe difference and pump-probe signals are visibly disproportionate.

The right column in Figure 5 shows calculated HHH-polarized pump-probe difference and HH-polarized pump-probe signals for $(\mathrm{TFMA})_2$. Control- and pump-pulse parameters are the same as those given earlier. For these simulations, which required a large basis set, we present only the stimulated-emission signals from an oriented sample having one site transition dipole in the H-direction and the other perpendicular to it. With the choice of a probe pulse with duration $\sigma_C = 333\,\mathrm{fs}$ having its center frequency electronically resonant from the bottom of the excited-state potential, we can anticipate that stimulated emission will entirely dominate the signals. Selected slices shown in the second panel of the right column are for t_{AP} = 500.3 fs (purple) and 900.5 fs (teal). Similar calculations in Paper 2 support an expectation that the signals from isotropic and oriented samples should differ only in small respects. As was seen in Figure 3 for this system,

the range of delays after the pump pulse up to 2 ps, about a half-period of excited-state torsional oscillation, displays the greatest sensitivity to the state of librational motion prior to electronic excitation (i.e., the greatest variability with t_{AP}). The pump-probe signal in the right-bottom panel is dissimilar in form to the pump-probe difference traces shown in the panel above it.

Concluding Comments

The influence of impulsive vibrational excitation upon short-time EET predicted for the systems considered here is short of complete on-off control, but it should be spectroscopically observable. Experiments along the lines envisaged here and in Papers 1 and 2 are likely to bring to light many interesting features of how vibrational dynamics affects the spatial transport of electronic excitation in multi-chromophore assemblies.[25–28] The most thorough characterization of these effects would likely combine impulsive excitation of coherent nuclear motion with state reconstruction by md-WPI or 2D ES.[62,63]

Several generalizations of the theoretical treatment and the experimental strategy naturally suggest themselves. Despite the care taken to choose control-pulse durations that efficiently excite a single nuclear mode, it remains necessary to incorporate vibrational relaxation and dephasing due to anharmonic coupling between the driven mode and other intramolecular or medium degrees of freedom, and the effects of these at nonzero temperatures. It would also be worthwhile to investigate the consequences for EET of selective or coordinated motion of a single mode or several modes, respectively, by an appropriately designed control-pulse *sequence*. Beyond the fluorinated methyl-group "control knobs" considered here, a wide variety of substituents that undergo significant torsional or vibrational displacement upon electronic excitation of the parent chromophore are likely to reward further investigation.[64] A more exhaustive exploration the effects of control-pulse chirp[65] or the direct excitation of IR-active vibrations with phase-controlled THz pulses is also desirable,[66] along with an examination of the influence of coherent vibrational motion on EET within the larger context of coherent-control theory.[67,68] Our study of vibrational control has focused on the influence of coherent intramolecular nuclear motion through its effect on EET surface-crossing

or, equivalently, the variation of instantaneous "donor emission" and "acceptor absorption" frequencies. It should also be possible to investigate the operation of this control mechanism in concert with the deliberate external variation of intermolecular coupling.[69–71]

Acknowledgment

This work was supported by US-NSF grant CHE-207190.

References

(1) J. D. Biggs and J. A. Cina, "Using wave-packet interferometry to monitor the external vibrational control of electronic excitation transfer," J. Chem. Phys. **131**, 224101/1-11 (2009).

(2) S. Mukamel, "Multidimensional femtosecond correlation spectroscopies of electronic and vibrational excitations," Annu. Rev. Phys. Chem. **51**, 691-729 (2000).

(3) M. Cho, *Two-Dimensional Optical Spectroscopy* (CRC Press, Boca Raton, 2009).

(4) P. Hamm and M. Zanni, *Concepts and Methods of 2D Infrared Spectroscopy* (Cambridge University Press, Cambridge, 2011).

(5) D. M. Jonas, "Two-dimensional femtosecond spectroscopy," Annu. Rev. Phys. Chem. **54**, 425-463 (2003).

(6) S. Rackovsky and R. Silbey, "Electronic energy transfer in impure solids I. Two molecules embedded in a lattice," Molec. Phys. **25**, 61-72 (1973).

(7) G. S. Schlau-Cohen, A. Ishizaki, and G. R. Fleming, "Two-dimensional electronic spectroscopy and photosynthesis: Fundamentals and applications to photosynthetic light-harvesting," Chem. Phys. **386**, 1–22 (2011).

(8) A. Ishizaki and G. R. Fleming, "Unified treatment of quantum coherent and incoherent hopping dynamics in electronic energy transfer: Reduced hierarchy equation approach," J. Chem. Phys. **130**, 234111/1-10 (2009).

(9) S. Jang, Y.-C. Cheng, D. R. Reichman, and J. D. Eaves, "Theory of coherent resonance energy transfer" J. Chem. Phys. **129**, 101104/1-4 (2008).

(10) G. Panitchayangkoon, D. Hayes, K. A. Fransted, J. R. Caram, E. Harel, J. Wen, R. E. Blankenship, and G. S. Engel, "Long-lived quantum coherence in photosynthetic complexes at physiological temperature," Proc. Natl. Acad. Sci. USA **107**, 12766-12770 (2010).

(11) D. B. Turner, K. E. Wilk, P. M. G. Curmi, and G. D. Scholes, "Comparison of electronic and vibrational coherence measured by two-dimensional electronic spectroscopy," J. Phys. Chem. Lett. **2**, 1904-1911 (2011).

(12) E. Collini, C. Y. Wong, K. E. Wilk, P. M. G. Curmi, P. Brumer, and G. D. Scholes, "Coherently wired light-harvesting in photosynthetic marine algae at ambient temperature," Nature **463**, 644-647 (2010).

(13) P. Huo and D. F. Coker, "Theoretical study of coherent excitation energy transfer in cryptophyte phycocyanin 645 at physiological temperature," J. Phys. Chem. Lett. **2**, 825–833 (2011).

(14) K. Gundogdu, K. W. Stone, D. B. Turner, and K. A. Nelson, "Multidimensional coherent spectroscopy made easy," Chem. Phys. **341**, 89-94 (2007).

(15) N. Christensson, F. Milota, J. Hauer, J. Sperling, O. Bixner, A. Nemeth, and H. F. Kauffmann, "High frequency vibrational modulations in two-dimensional electronic spectra and their resemblance to electronic coherence signatures," J. Phys. Chem. B **115**, 5383–5391 (2011).

(16) J. A. Myers, K. L. M. Lewis, F. D. Fuller, P. F. Tekavec, C. F. Yocum, and J. P. Ogilvie, "Two-

dimensional electronic spectroscopy of the D1-D2-cyt b559 photosystem II reaction center complex," J. Phys. Chem. Lett. **1**, 2774–2780 (2010).

(17) G. A. Lott, A. Perdomo-Ortiz, J. K. Utterback, A. Aspuru-Guzik, and A. H. Marcus, "Conformation of self-assembled porphyrin dimers in liposome vesicles by phase-modulation 2D fluorescence spectroscopy," Proc. Nat. Acad. Sci. (2011, in press).

(18) D. Brinks, F. D. Stefani, F. Kulzer, R. Hildner, T. H. Taminiau, Y. Avlasevich, K. Müllen, and N. F. van Hulst, "Visualizing and controlling vibrational wave packets of single molecules, Nature **465**, 905-908 (2010).

(19) J. M. Womick and A. M. Moran, "Vibronic enhancement of exciton sizes and energy transport in photosynthetic complexes," J. Phys. Chem. B **115**, 1347–1356 (2011).

(20) B. A. West, J. M. Womick, L. E. McNeil, K. J. Tan, and A. M. Moran, "Influence of vibronic coupling on band structure and exciton self-trapping in α-perylene," J. Phys. Chem. B **115**, 5157–5167 (2011).

(21) D. Segale and V. A. Apkarian, "Dissipative quantum coherent dynamics probed in phase-space: Electronically resonant 5-color 4-wave mixing on I_2(B) in solid Kr," J. Chem. Phys. **135**, 024203/1-12 (2011).

(22) D. Egorova, "Detection of electronic and vibrational coherences in molecular systems by 2D electronic photon echo spectroscopy," Chem. Phys. **347**, 166-176 (2008).

(23) A. Schubert and V. Engel, "Two-dimensional vibronic spectroscopy of coherent wave-packet motion," J. Chem. Phys. **134**, 104304/1-8 (2011).

(24) E. R. Smith and D. M. Jonas, "Alignment, vibronic level splitting, and coherent coupling effects on the pump-probe polarization anisotropy," J. Phys. Chem. A **115**, 4101–4113 (2011).

(25) M. Mohseni, P. Rebentrost, S. Lloyd, and A. Aspuru-Guzik, "Environment-assisted quantum walks in photosynthetic energy transfer," J. Chem. Phys. **129**, 174106/1-9 (2008).

(26) P. Rebentrost, M. Mohseni, and A. Aspuru-Guzik, "Role of quantum coherence and environmental fluctuations in chromophoric energy transport," J. Phys. Chem. B **113**, 9942-9947 (2009).

(27) M. B. Plenio and S. F. Huelga, "Dephasing-assisted transport: quantum networks and biomolecules," New J. Phys. **10**, 113019/1-14 (2008).

(28) F. Caruso, A. W. Chin, A. Datta, S. F. Huelga, and M. B. Plenio, "Highly efficient energy excitation transfer in light-harvesting complexes: The fundamental role of noise-assisted transport," J. Chem. Phys. **131**, 105106/1-15 (2009).

(29) J. D. Biggs and J. A. Cina, "Calculations of nonlinear wave-packet interferometry signals in the pump-probe limit as tests for vibrational control over electronic excitation transfer," J. Chem. Phys. **131**, 224302/1-12 (2009).

(30) I. Yamazaki, S. Akimoto, T. Yamazaki, S. Sato, and Y. Sakata, "Oscillatory excitation transfer in dithiaanthracenophane: Quantum beat in a coherent photochemical process in solution," J. Phys. Chem. A **106**, 2122-2128 (2002); I. Yamazaki, S. Akimoto, N. Aratani, and A. Osuka, "Observation of coherent recurrence motion of excitons in anthracene dimers," Bull. Chem. Soc. Jpn. **77**, 1959-1971 (2004).

(31) L. Yang, S. Caprasecca, B. Mennucci, and S. Jang, "Theoretical investigation of the mechanism and dynamics of intramolecular coherent resonance energy transfer in soft molecules: A case study of dithia-anthracenophane," J. Am. Chem. Soc. **132**, 16911–16921 (2010).

(32) Ref. 29, Sec. II B.

(33) Ref. 29, Appendix.

(34) J. D. Biggs, *Theoretical Studies of the External Vibrational Control of Electronic Excitation Transfer and Its Observation Using Polarization- and Optical Phase-sensitive Ultrafast Spectroscopy*, Ph.D. dissertation, University of Oregon, Eugene, Oregon (2010).

(35) Ref. 29, Sec. II A.

(36) Y. C. Shen and J. A. Cina, "What can short-pulse pump-probe spectroscopy tell us about Franck-Condon dynamics?" J. Chem. Phys. **110**, 9793-9806 (1999).

(37) For unsubstituted DTA, a Frenkel-exciton picture finds justification in the results of Ref. 31, page 16914.

(38) W. R. Lambert, P. M. Felker, J. A. Syage, and A. H. Zewail, "Jet spectroscopy of anthracene and deuterated anthracenes," J. Chem. Phys. **81**, 2195-2208 (1984).

(39) L. Dhar, J. A. Rogers, and K. A. Nelson, "Time-resolved vibrational spectroscopy in the impulsive limit," Chem. Rev. **94**, 157-193 (1994).

(40) K. Ohno, "Normal coordinate calculations of benzenoid hydrocarbons. Theoretical models of simplified valence force fields," J. Mol. Spectrosc. **72**, 238-251 (1978); K. Ohno, "Normal coordinate calculations of benzenoid hydrocarbons. Classification and characterization of aromatic planar vibrations in polyacenes," J. Mol. Spectrosc. **77**, 329-348 (1979).

(41) H. Lin, J. A. Hunter, and J. Pfab, "Laser-induced fluorescence spectroscopy of jet-cooled 2-methylanthracene S_1 (π, π^*) - evidence for methyl conformation change upon electronic excitation," Chem. Phys. Lett. **210**, 38-44 (1993). See also: X.-Q. Tan, W. A. Majewski, D. F. Plusquellic, and D. W. Pratt, "Methyl group torsional dynamics from rotationally resolved electronic spectra. 1- and 2-methylnaphthalene," J. Chem. Phys. **94**, 7721-7733 (1991); H. Nakai and Y. Kawamura, "π^*–σ^* Hyperconjugation mechanism on the rotational barrier of the methyl group (II): 1- and 2-methylnaphthalenes in the S_0, S_1, C_0, and A_1 states," Chem. Phys. Lett. **318**, 298–304 (2000).

(42) M. Nakagaki, E. Nishi, K. Sakota, K. Nishi, H. Nakano, and H. Sekiya, "Internal rotation of methyl group in 2- and 1-methylanthracene studied by electronic spectroscopy and DFT calculations," Chem. Phys. **316**, 178-184 (2005).

(43) M. J. Frisch, G. W. Trucks, H. B. Schlegel, et al., *Gaussian 09, Revision A.02* (Gaussian, Inc., Wallingford, 2009).

(44) R. G. Parr and W. Yang, *Density-Functional Theory of Atoms and Molecules in Chemistry* (Springer, New York, 1991).

(45) A. D. Becke, "Density-functional thermochemistry III. The role of exact exchange," J. Chem. Phys. **98**, 5648-5652 (1993).

(46) T. H. Dunning, "Gaussian basis sets for use in correlated molecular calculations I. The atoms boron through neon and hydrogen," J. Chem. Phys. **90**, 1007-1023 (1989).

(47) E. Runge and E. K. U. Gross, "Density-functional theory for time-dependent systems," Phys. Rev. Lett. **52**, 997–1000 (1984).

(48) R. Ditchfield, W. J. Hehre, and J. A. Pople, "Self-consistent molecular orbital methods. 9. Extended Gaussian-type basis for molecular-orbital studies of organic molecules," J. Chem. Phys. **54**, 724-728 (1971).

(49) In Eqs. (5) and (6) we use directly the spectroscopic value for J_{DTA}, and do not remove the mode-12 Franck-Condon overlap as is done the constructing the DTA-12 model.

(50) See Sec. I of Paper 2 for more details.

(51) S. Jang, Y. J. Jung, and R. J. Silbey, "Nonequilibrium generalization of Förster-Dexter theory for excitation energy transfer," Chem. Phys. **275**, 319–332 (2002).

(52) J. A. Cina and G. R. Fleming, "Vibrational coherence transfer and trapping as sources for long-lived quantum beats in polarized emission from energy transfer complexes," J. Phys. Chem. A **108**, 11196-11208 (2004).

(53) These figures were 5.0% for DTA-12, 4.8% for DFMA, and 7.0% for TFMA.

(54) The optimal chirp parameter is smaller in magnitude than the value ($-\sigma_P^2 = -357.2\,\mathrm{fs}^2$) that would produce the most rapid frequency downshift ($-1/(2\sigma_P^2) = -1.40\times10^{-3}\,\mathrm{rad\,fs}^{-2}$) consistent with the spectral bandwidth of an unchirped source pulse.

(55) Since ISRS does not induce a coherent librational displacement in TFMA, its control-pulse parameters were chosen by maximizing the librational energy of the second-order wave packet in the electronic ground state, subject to the population constraint mentioned earlier.

(56) In the notation of Papers 1 and 2, the state-1 amplitude is given by $\left|\psi_1(t)\right\rangle = [t - t_A]_{11} p_A^{(10)}(\infty;\tau)[t_{AP}]_{00} p_P^{(01)}(\infty;\tau') p_P^{(10)}(\tau';\tau'')[-t_{AP}]_{00}\left|(0_a 0_b)_0\right\rangle$.

(57) Compare Fig. 6 of Paper 2.

(58) For the sake of simplicity, we assume, in particular, that fluorescence from state 2 can be spectrally separated or is otherwise eliminated. With experimental information on the relative fluorescence quantum yields of various singly and multiply excited states, it would be straightforward to include the weighted contributions from other participating electronic levels. See Ref. 17 for a detailed discussion on this point.

(59) F. Ding, E. C. Fulmer, and M. T. Zanni, "Heterodyned fifth-order two-dimensional IR spectroscopy: Third-quantum states and polarization selectivity," J. Chem. Phys. **123**, 094502/1-13 (2005).

(60) One of which—the bra or the ket—contributes trilinearly in the pump and probe fields (proportionally to $E_A^2 E_C$ or $E_A E_C^2$), the other of which contibutes linearly (proportionally to E_C or E_A). See online Appendix C to Paper 1 for a complete list of contributing overlaps.

(61) See also Eq. (42) of Paper 1.

(62) T. S. Humble and J. A. Cina, "Nonlinear wave-packet interferometry and molecular state reconstruction in a vibrating and rotating diatomic molecule," J. Phys. Chem. B **110**, 18879-18892 (2006).

(63) J. Yuen-Zhou and A. Aspuru-Guzik, "Quantum process tomography of excitonic dimers from two-dimensional electronic spectroscopy. I. General theory and application to homodimers," J. Chem. Phys. **134**, 134505/1-19 (2011); J. Yuen-Zhou, J. J. Krich, M. Mohseni, and A. Aspuru-Guzik, "Quantum state and process tomography of energy transfer systems via ultrafast spectroscopy," Proc. Nat. Acad. Sci. (2011, in press).

(64) R. G. Bird, A. E. Nikolaev, and D. W. Pratt, "Microwave and UV excitation spectra of 4-fluorobenzyl alcohol at high resolution. S_0 and S_1 structures and tunneling motions along the low frequency $-CH_2OH$ torsional coordinate in both electronic states," J. Phys. Chem. A (2011, in press).

(65) A. Wand, S. Kallush, O. Shoshanim, O. Bismuth, R. Kosloff, and S. Ruhman, "Chirp effects on impulsive vibrational spectroscopy: a multimode perspective," Phys. Chem. Chem. Phys. **12**, 2149–2163 (2010).

(66) C. A. Schmuttenmaer, "Exploring dynamics in the far-infrared with terahertz spectroscopy," Chem. Rev. **104**, 1759-1779 (2004).

(67) S. A. Rice and M. Zhao, *Optical Control of Molecular Dynamics* (John Wiley & Sons, New York, 2000).

(68) M. Shapiro and P. W. Brumer, *Principles of the Quantum Control of Molecular Processes* (John Wiley & Sons, Hoboken, 2003).

(69) S. Jang, "Generalization of the Förster resonance energy transfer theory for quantum mechanical modulation of the donor-acceptor coupling," J. Chem. Phys. **127**, 174710/1-10 (2007).

(70) J. Cao and R. J. Silbey, "Optimization of exciton trapping in energy transfer processes," J. Phys. Chem. A **113**, 13827-13838 (2009).

(71) D. N. Beratan, S. S. Skourtis, I. A. Balabin, A. Balaeff, S. Keinan, R. Venkatramani, and D. Xiao, "Steering electrons on moving pathways," Acc. Chem. Res. **42**, 1669-1678 (2009).